

Study on Ground-Penetrating Radar (GPR) Application in Pavement Deep Distress Detection

Songtao Li^{1,2}, Chengchao Guo^{1,3*}

¹College of Water Conservancy and Environment, Zhengzhou University, Zhengzhou, China

²Industrial Technology Research Institute, Chongqing University, Chongqing, China

³School of Civil Engineering, Sun Yat-sen University, Guangzhou, China

Email: *wangchench@163.com

How to cite this paper: Li, S.T. and Guo, C.C. (2019) Study on Ground-Penetrating Radar (GPR) Application in Pavement Deep Distress Detection. *Journal of Transportation Technologies*, 9, 232-259.
<https://doi.org/10.4236/jtts.2019.92015>

Received: March 22, 2019

Accepted: April 25, 2019

Published: April 29, 2019

Copyright © 2019 by author(s) and Scientific Research Publishing Inc. This work is licensed under the Creative Commons Attribution International License (CC BY 4.0).

<http://creativecommons.org/licenses/by/4.0/>



Open Access

Abstract

As some deep distresses exist in pavement structures, ground-penetrating radar (GPR) reflected waves will vary at interfaces and defects. Aimed at detecting the distresses in terms of position, severity and degree, electromagnetic forward simulations based on 400 MHz and 900 MHz antennas were conducted respectively. The dielectric models concerning homogeneous or coupling distresses of pavements were established, and the effects of various distresses on detection were analyzed through reflected wave images. Relying on GPR tests and field tests, coring and excavation data acquired before rehabilitation were compared and verified. The calculation results match the field measurement results. Thus, the detection method based on GPR was proposed for pavement deep distresses.

Keywords

Pavement, Deep Distress, GPR, Electromagnetic Forward Simulation, Dielectric Model, Detection

1. Introduction

Ground-penetrating radar (GPR) was designed specifically to penetrate the ground surface and inspect the subsurface by locating abnormality. Currently, it was utilized in many fields as a non-destructive detection method [1].

For the evaluation of subgrade soil in road structures, GPR-related methods were adopted to nondestructively identify soil types and estimate the thickness of overburden layer, the compressibility and frost susceptibility of subgrade soil [2]. For pavement structures, GPR was used to measure the thickness of each

layer, detect subsurface defects and evaluate the quality of base course [3]. For quality control surveys, thickness measurement could be performed with GPR to estimate air void content of asphalt surface and detect mix segregation [4]. Besides, through GPR detection, pavement pumping could be predicted [5]. Based on microwave technology for free space measurement, this paper developed and introduced a GPR mixed model to determine the density of pavement structures [6]. Through observations and modelling, GPR could perform effectively in characterizing and detecting vertical pavement cracks, and a multi-frequency GPR approach to pavement detection was recommended, *i.e.*, 900 MHz for crack characterization and low frequency for crack detection [7]. Through various practices (e.g., laboratory tests, the long-term visual observation, repeated GPR scanning and probed drillings), investigations of pavement transversal cracks with GPR methods were presented [8].

Generally, GPR applications were involved in various related tests and pavement structures evaluation, mainly including pavement quality control, stripping detection in bituminous materials, layer thickness determination, position determination of structural variations and voids, evaluation of excess moisture beneath bound layers and the determination of depth and alignment of steelwork [9], etc.

As layered structures, pavements are designed to carry traffic loads. Various defects (e.g., rutting, stripping, cracking and poor bonding) in pavement structures will create changes to GPR images under repeated traffic loads, different temperatures and humidity. According to the above, deep defects in pavement structures can be detected.

In this paper, the numerical simulations and field tests for GPR application in pavement deep distresses detection will be performed. Besides, a case study will be conducted, which may provide a reference for design, construction, maintenance and rehabilitation of pavements.

2. Numerical Simulation

First, confirm that you have the correct template for your paper size. This template has been tailored for output on the custom paper size (21 cm × 28.5 cm). Finite Difference Time Domain (FDTD) method can be classified as a high-frequency electromagnetic field simulation method. It has been exerted widely in forward simulation of GPR electromagnetic wave propagation. Based on the principles of Maxwell's equations and results obtained by James and Rosemary [10], the model and PML absorbing boundary conditions have been modified. According to different frequencies, the different time window has been set, and the reflection waves derived from 400 MHz and 900 MHz ground-coupled antennas have been forward simulated to verify validity and reliability of GPR in detecting pavement deep distresses. It starts by presetting defects in pavement deep layers. Then, GPR transmits signals across the abnormal position, and reflected waves will be recorded. Thus, in contrast with the simu-

lated spectrum, the defect can be detected.

Pavement structures consist of several layers, as shown in **Table 1**. Regarding various pavement materials, the dielectric permittivity ε , magnetic permeability μ , and electrical conductivity σ present different values. Generally, as pavement materials are non-magnetic, magnetic permeability μ is set as 1. The dielectric permittivity ε and electrical conductivity σ are equivalent in real part and imaginary part of dielectric constant in Maxwell equation respectively. Thus, the value of ε and σ can be determined. As asphalt concrete shows similar dielectric properties, the three surface layers can be simplified as a layer. The typical dielectric values for each layer are listed in **Table 1**. In this model, median value is adopted as the dielectric constant.

The dielectric model of pavement structure layers can be established. Within each layer, there may exist several abnormal zones of different dimensions indicating defects respectively. The defects create changes to the values of ε and σ for different pavement structures.

In the simulation, 8 typical road structural diseases were selected as representatives. The selected cases may be not quite comprehensive, while it may help reveal the feasibility of GPR application in pavement deep distress detection. Besides, through comparison of the simulation results of 400 MHz and 900 MHz under different cases, the respective advantage of the two antennas could be presented.

2.1. Antenna Simulation of 400 MHz

In some cases, accurate imaging of the target defects may not be obtained through 400 MHz antenna from the surface course. Dead zones will hinder the detection of targets, while high-accuracy detection still cannot be maintained without dead zones in the test structures. Combined with the real pavement structures, the homogeneous dielectric model is set up. The length and depth of 400 MHz (*i.e.*, center frequency) antenna simulation model is 5 m and 2 m respectively, and the latter lies in the detection depth range (*i.e.*, 0 - 4 m) of 400 MHz ground-coupled antenna according to the device parameters of selected GPR. Besides, the time window is set as 25 ns. Although some dielectric properties (e.g., dispersion) are not involved in uniform supposition, GPR numerical model can be utilized to reveal the relation between subsurface properties and GPR data. Thus, the related mechanism of GPR detection may be acquired. It can also be analyzed at a fraction of computation with more effective algorithms.

In the model, an air-surface interface is fixed at $z = 0$, which is achieved by adding a 50 cm thick air layer with $\varepsilon = 1$ and $\sigma = 0$ to the grid. Sources and receivers are placed along the air-surface interface every 0.1 m for reflection investigation. The Blackman-Harris source pulses possess a dominant frequency of 400 MHz. As to the pulse and the dielectric properties in the pavement model, the spatial and time steps are set as 0.01 m and 0.02 ns, respectively.

Table 1. Pavement material and dielectric value.

Layer	Main Parameters			
	Table column subhead	ϵ	μ	σ
1	4 cm fine-grained asphalt concrete (AC-13C)			
2	6 cm medium-grained asphalt concrete (AC-20C)	4 - 8	1	0.01 - 0.1
3	8 cm coarse-grained asphalt concrete (ATB-30)			
4	40 cm cement stabilized gravel base	8 - 12	1	0 - 1
5	15 cm cement stabilized gravel subbase	10 - 20	1	0 - 0.2
6	semi-infinite subgrade	10 - 30	1	0 - 0.02

The dielectric model with various simulated defects is established, and the defects vary with the type, depth and dimension. The sources are placed before the receiver at a certain spacing. As source waves propagate at a velocity in the pavement structure, the wave will be recorded by receivers.

In practice, pavement performance is undermined mainly due to surface defects, and secondary surface may be generated due to deep distresses, e.g., inner undercompacted and void zones. Relying on its distinguished precision, GPR is widely applied in the qualitative detection of various defects. Therefore, in the simulation, it should be investigated whether distresses could be detected and that whose dimension is secondary.

Case 1: The dielectric model of pavement with locally undercompacted surface course is shown in **Figure 1(a)**, and several layers are contained in the model, *i.e.*, air layer, surface course, base course, subbase course and subgrade. Three undercompacted zones are presented in surface course with the dimension of 1 cm \times 1 cm, 1 cm \times 3 cm and 1 cm \times 5 cm respectively, and the corresponding reflected wave image is illustrated in **Figure 1(b)**.

Case 2: The dielectric model of pavement with voids in the bottom of surface course is shown in **Figure 2(a)**, and the defect dimension was 5 cm \times 50 cm. Voids were filled with air, and the corresponding reflected wave is illustrated in **Figure 2(b)**.

Case 3: The dielectric model of pavement with voids in the bottom of surface course is shown in **Figure 3(a)**, and the defect dimension was 5 cm \times 50 cm. Voids were filled with water, and the corresponding reflected wave is illustrated in **Figure 3(b)**.

As can be seen from **Figures 1-3**, when electromagnetic waves propagated into the dielectric model with voids or undercompacted zones, the reflected wave images would report the variation at the position with defects. Particularly, defects with relatively smaller dimension, e.g., 1 cm \times 1 cm in **Figure 1(a)**, could be detected with acquired reflected waves. Due to the close range between two

defects, the reflected waves interfered mutually, and a superposed wave was generated. Moreover, with the larger dimension of models shown in **Figure 2** and **Figure 3**, stronger reflected waves were obtained. As the dielectric constant increased with the presence of moisture, stronger reflected waves appeared, as shown in **Figure 3**.

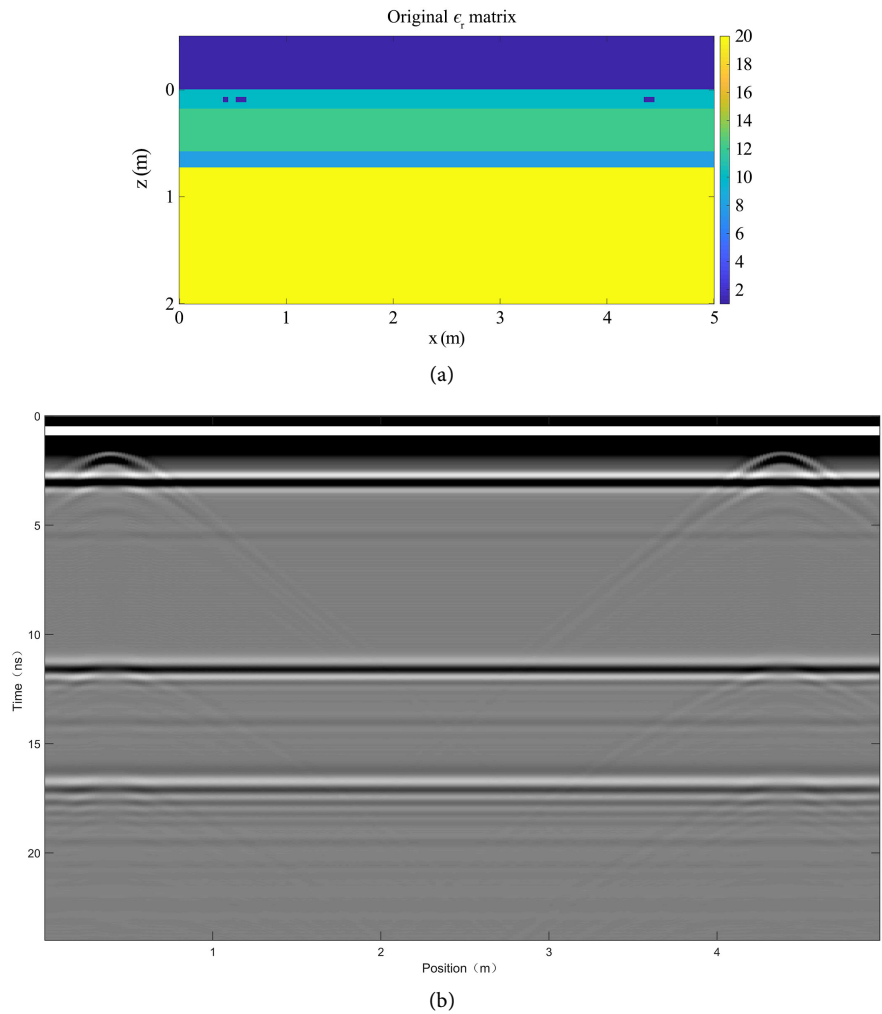
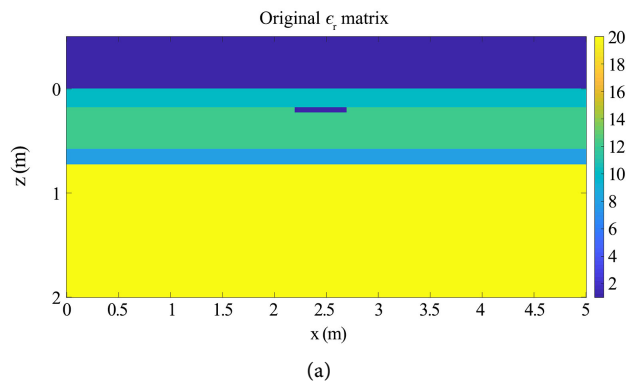
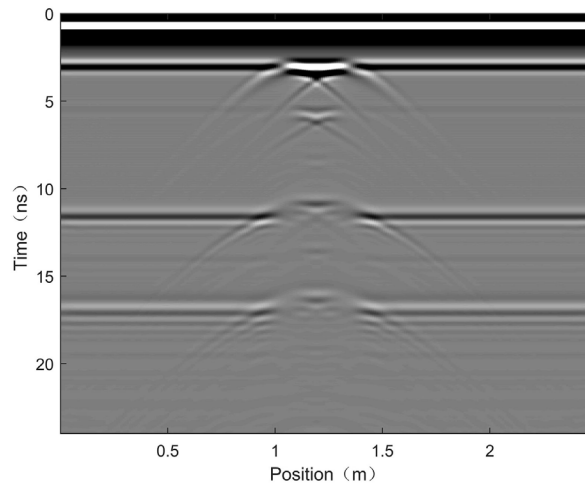


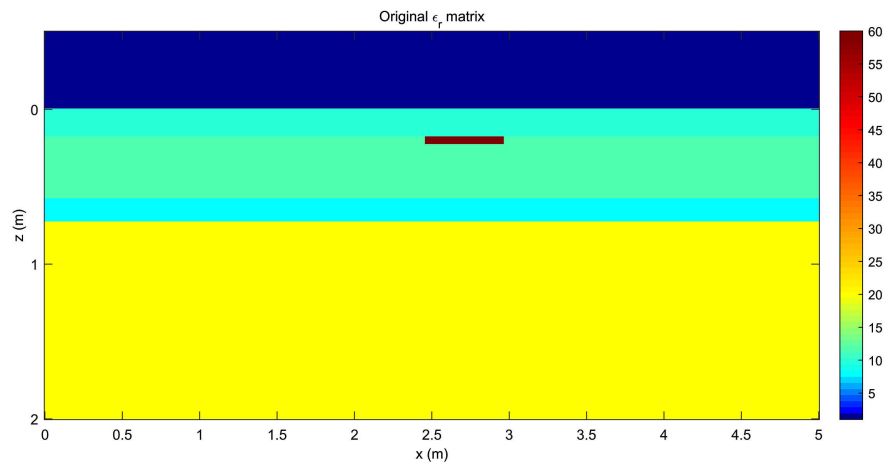
Figure 1. (a) Dielectric model of pavement with locally undercompacted surface course; (b) Reflected wave of model 1a.



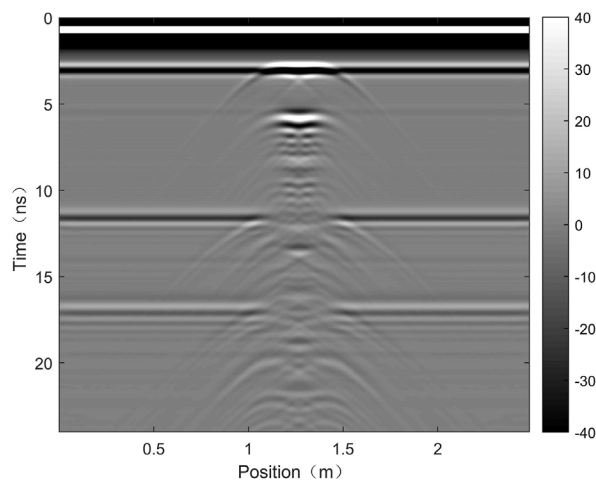


(b)

Figure 2. (a) Dielectric model of pavement with voids filled with air in surface course; (b) Reflected wave of model 2a.



(a)



(b)

Figure 3. (a) Dielectric model of pavement with voids filled with water in surface course; (b) Reflected wave of model 3a.

Case 4: The dielectric model of pavement with locally undercompacted base is shown in **Figure 4(a)**, and the defect dimensions were 1 cm \times 1 cm and 1 cm \times 10 cm. The corresponding reflected wave is shown in **Figure 4(b)**.

Case 5: The dielectric model of pavement with voids in the base bottom is shown in **Figure 5(a)**, and the defect dimension was 5 cm \times 50 cm. Voids were filled with air, and the corresponding reflected wave is illustrated in **Figure 5(b)**.

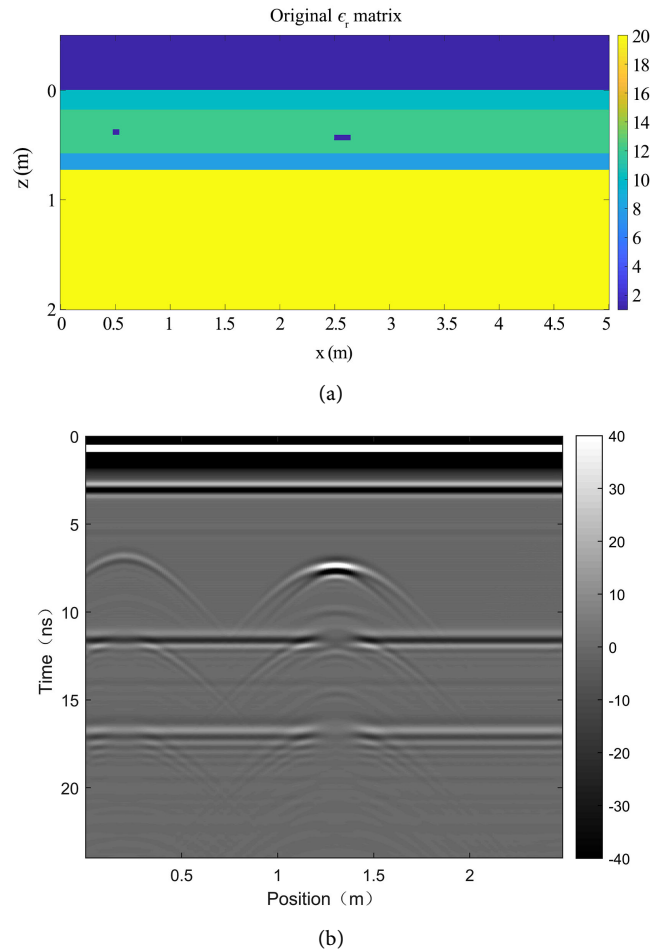
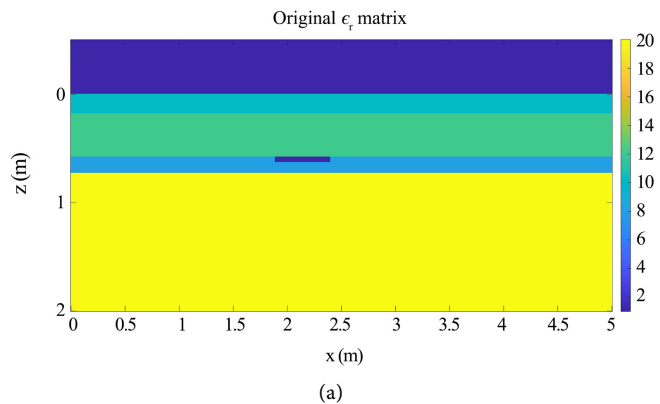


Figure 4. (a) Dielectric model of pavement with voids filled with water in surface course; (b) Reflected wave of model 4a.



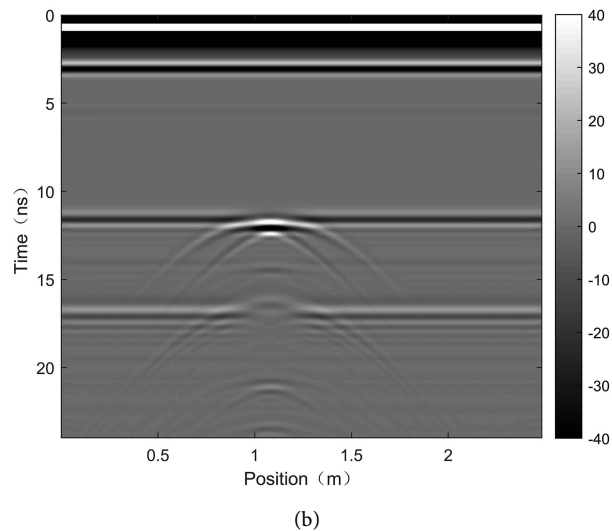


Figure 5. (a) Dielectric model of pavement with voids filled with water air in base; (b) Reflected wave of model 5a.

Case 6: The dielectric model of pavement with voids in the base bottom is shown in **Figure 6(a)**, and the dimension of defect was $5\text{ cm} \times 50\text{ cm}$. Voids were filled with water, and the corresponding reflected wave is illustrated in **Figure 6(b)**.

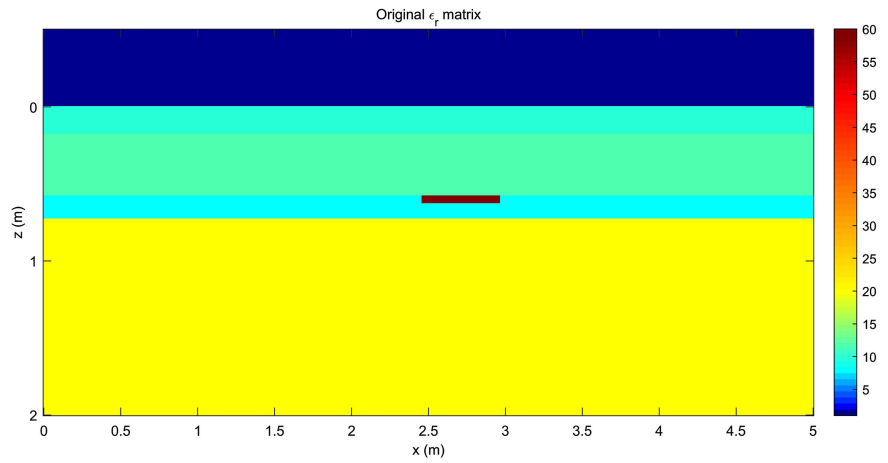
It can be seen from **Figures 4-6** that reflected images varied with the width and length of voids or undercompacted zones in base. The scope and area could be quantitatively identified based on the images approximately. The reflected waves varied from weak to strong as the voids became filled with water instead of air, and the intensity of reflected waves induced by undercompacted zones lay between that of the two cases. If two defects were at a certain spacing, reflected maps could not interfere mutually, e.g., Case 4.

Case 7: The dielectric model of pavement with locally undercompacted sub-base is shown in **Figure 7(a)**, and the defect dimensions were $1\text{ cm} \times 1\text{ cm}$, $1\text{ cm} \times 3\text{ cm}$ and $1\text{ cm} \times 3\text{ cm}$ respectively at different positions. The corresponding reflected image is shown in **Figure 7(b)**. With regard to **Figure 7**, it is supposed that three defects were located in subbase course, and three abnormal reflections could be identified at corresponding positions.

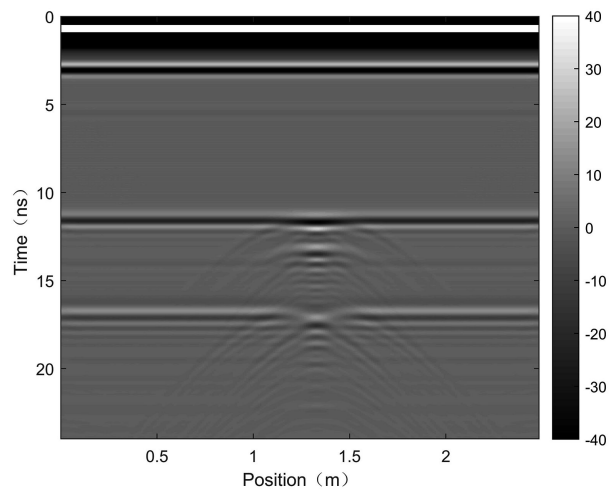
Case 8: The coupled dielectric model of pavement with coupled voids in surface course and base bottom. The voids were filled with air and water respectively, as shown in **Figure 8(a)**, and the void dimension was $5\text{ cm} \times 50\text{ cm}$. The corresponding reflected wave is shown in **Figure 8(b)**. The different positions cannot be identified by abnormal reflection, while the coupled distresses could be revealed through the image. Besides, the defect property could also be investigated by reflection intensity briefly.

Thus, the conclusion can be drawn that regardless of the position of voids or undercompacted zones in each layer, the reflected wave images varied with the defect with a certain dimension. The established models may interfere mutually

or be coupled, while the defect still could be identified through the abnormal reflected wave images. The strongest parts of reflection waves existed in the central position of defects, which could be recognized from the forward simulation images.

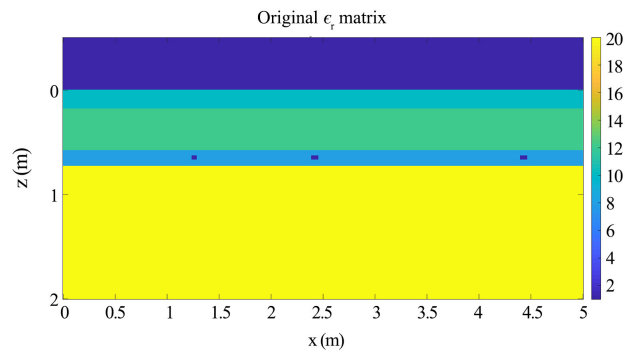


(a)



(b)

Figure 6. (a) Dielectric model of pavement with voids filled with water air in base; (b) Reflected wave of model 6a.



(a)

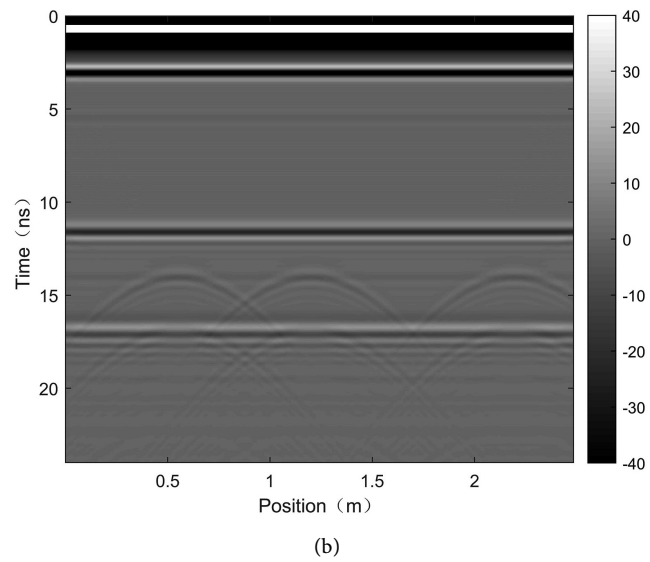


Figure 7. (a) Dielectric model of pavement with locally undercompacted subbase; (b) Reflected wave of model 7a.

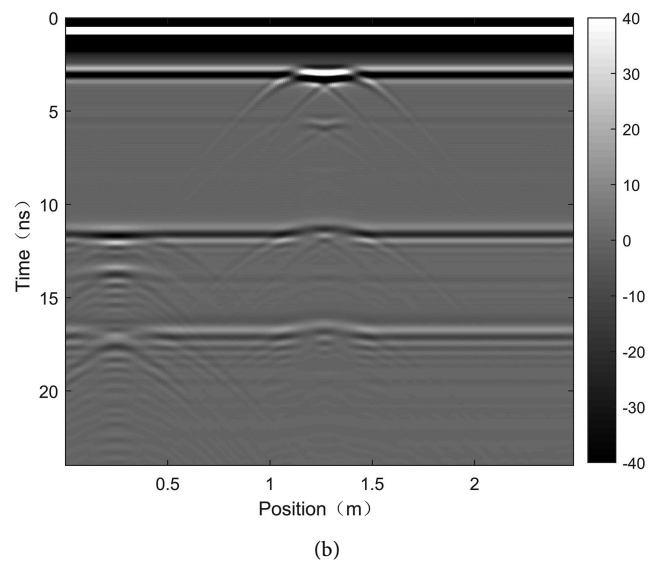
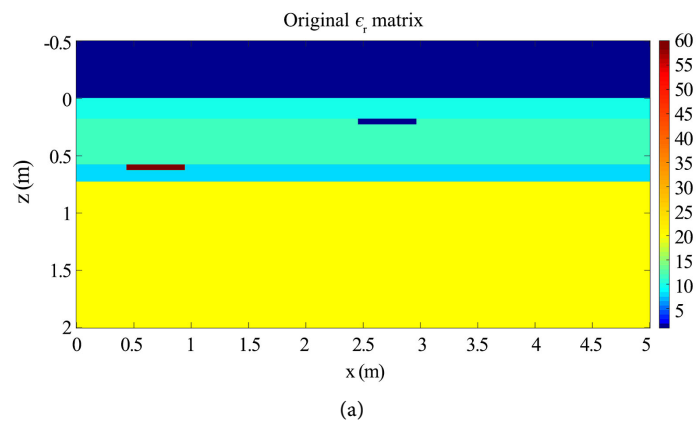


Figure 8. (a) Dielectric model of pavement with coupled voids in surface course and base bottom; (b) Reflected wave of model 8a.

2.2. Antenna Simulation of 900 MHz

Based on real pavement structures, the electromagnetic wave dielectric model is set up. Within the layers, one or several anomalous blocks of defect were created with different dimensions respectively. Similar with antenna simulation of 400 MHz, the length and depth of 900 MHz (*i.e.*, center frequency) antenna simulation model are 1.4 m and 0.75 m. The latter lies in the detection depth range (*i.e.*, 0 - 1 m) of 900 MHz ground-coupled antenna according to the device parameters of selected GPR, and the time window is set as 15 ns.

In the model, an air-surface interface is fixed at $z = 0$, which is achieved by simply adding a 25 cm thick air layer with $\varepsilon = 1$ and $\sigma = 0$ to the grid. Sources and receivers are placed along the air-surface interface every 0.05 m for reflection investigation. The Blackman-Harris source pulses possess a dominant frequency of 900 MHz. As to the pulse and dielectric properties in the pavement model, the spatial and time steps are set as 0.005 m and 0.01 ns, respectively.

Similar with 400 MHz antenna simulation, the model is established, and source waves propagate in pavement structures and then will be recorded by receivers.

Case 1: The dielectric model of pavement with locally undercompacted zones in the surface course top is shown in **Figure 9(a)**. Two undercompacted zones were contained with the dimension of 1 cm \times 1 cm and 1 cm \times 3 cm respectively, and the corresponding reflected wave image is shown in **Figure 9(b)**. With the same defect dimension, the range of the reflected wave was larger than that of 400 MHz. Thus, based on 900 MHz antenna, the detection with higher accuracy could be obtained, *i.e.*, smaller defects could also be identified generally.

Case 2: The dielectric model of pavement with locally undercompacted zones in the intermediate surface course is shown in **Figure 10(a)**. The two small undercompacted zones were contained with the dimension of 0.5 cm \times 10 cm and 0.25 cm \times 5 cm respectively. The corresponding reflected wave image is shown in **Figure 10(b)**. Although the target defects became smaller, they still could be detected through the reflected wave image with higher frequency propagation.

Case 3: The dielectric model of pavement with locally undercompacted zones in the surface course bottom is shown in **Figure 11(a)**. Two undercompacted zones existed with the dimension of 0.5 cm \times 5 cm and 0.25 cm \times 10 cm respectively, and the corresponding reflected wave image is shown in **Figure 11(b)**. Defects position and the dimension (*i.e.*, width and length) of the model in the Case 3 varied compared with that Case 2, while the simulation images were similar acquired in Case 2 and 3.

Case 4: The dielectric model of pavement with locally undercompacted zones in the base top is shown in **Figure 12(a)**. Three abnormal zones were contained with the dimension of 0.5 cm \times 3 cm, 0.5 cm \times 5 cm and 1 cm \times 1 cm respectively, and the corresponding reflected wave image is shown in **Figure 12(b)**.

Case 5: The dielectric model of pavement with locally undercompacted zones in the base bottom is shown in **Figure 13(a)**. Two undercompacted zones ex-

isted with the dimension of $0.25 \text{ cm} \times 3 \text{ cm}$ and $1 \text{ cm} \times 1 \text{ cm}$ respectively, and the corresponding reflected wave image is shown in **Figure 13(b)**.

It is shown that the detection depth of 900 MHz decreased, while the detection accuracy increased, higher than that of 400 MHz. Therefore, the target defects contained in deeper layers, could also be identified through reflected wave images, e.g., **Figure 12(b)** and **Figure 13(b)**.

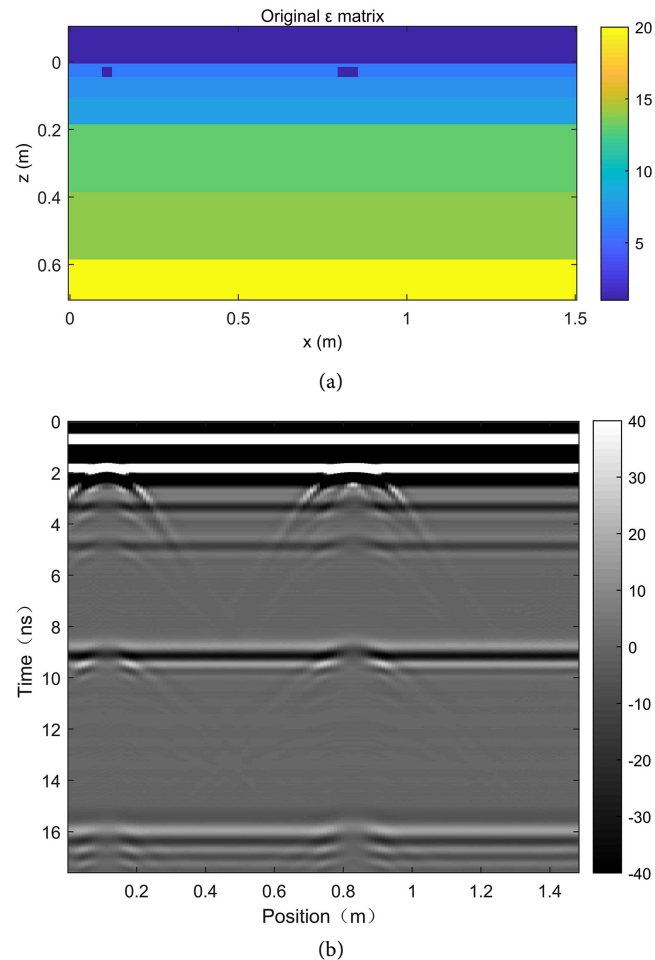
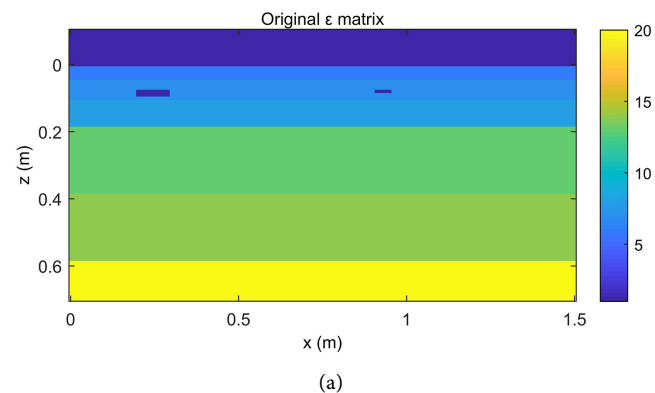


Figure 9. (a) Dielectric model of pavement with undercompacted surface top; (b) Reflected wave of model 9a.



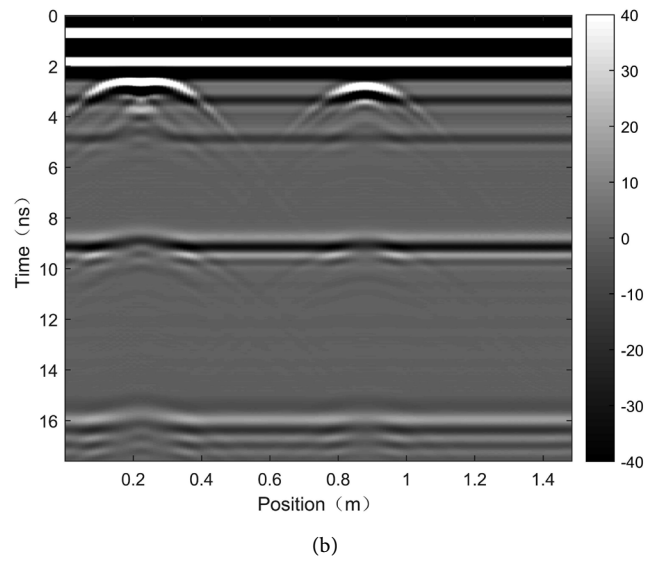


Figure 10. (a) Dielectric model of pavement with undercompacted intermediate surface; (b) Reflected wave of model 10a.

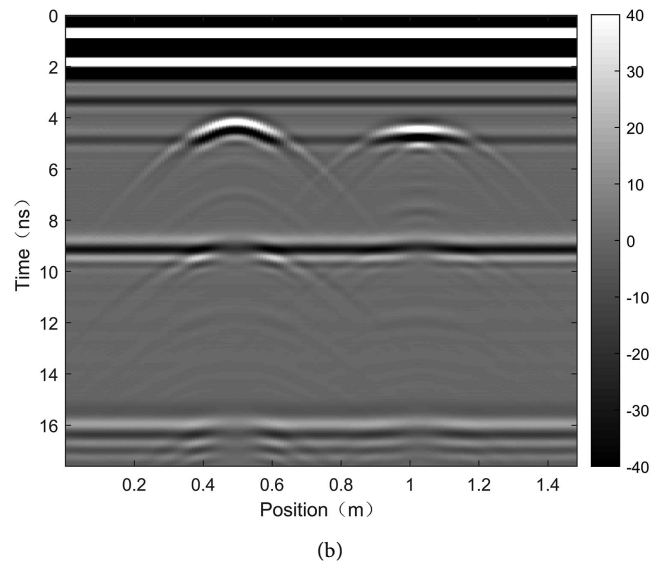
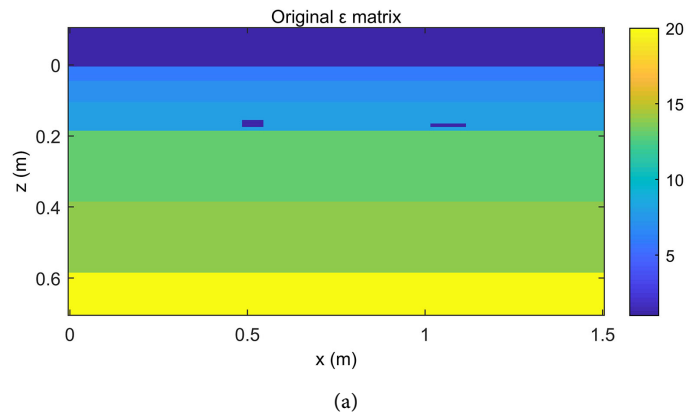
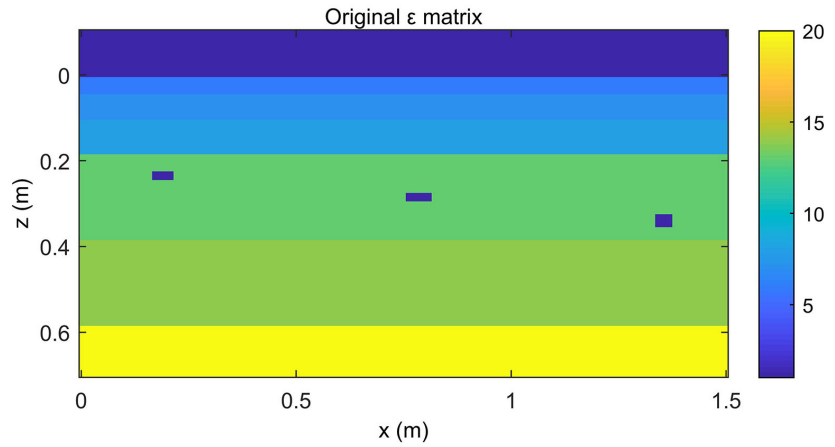
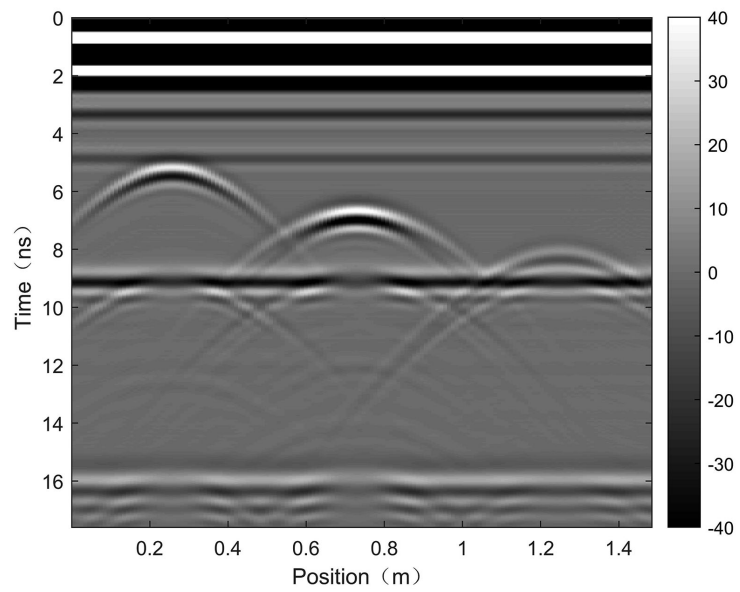


Figure 11. (a) Dielectric model of pavement with undercompacted surface bottom; (b) Reflected wave of model 11a.

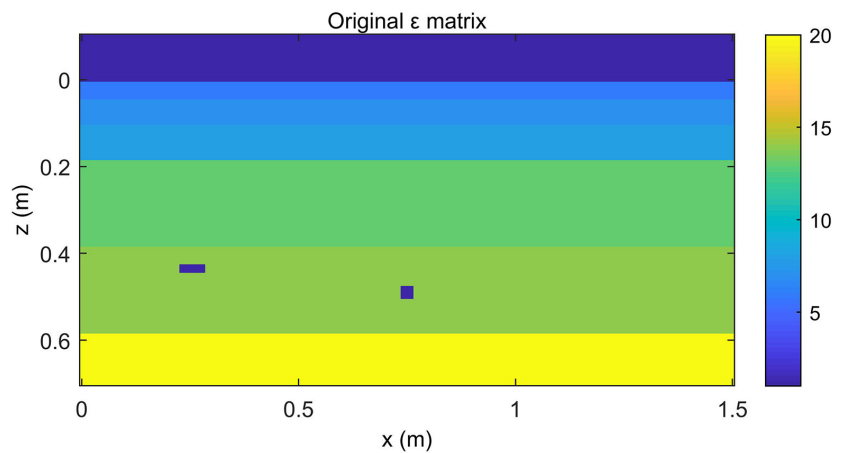


(a)



(b)

Figure 12. (a) Dielectric model of pavement with undercompacted base top; (b) Reflected wave of model 12a.



(a)

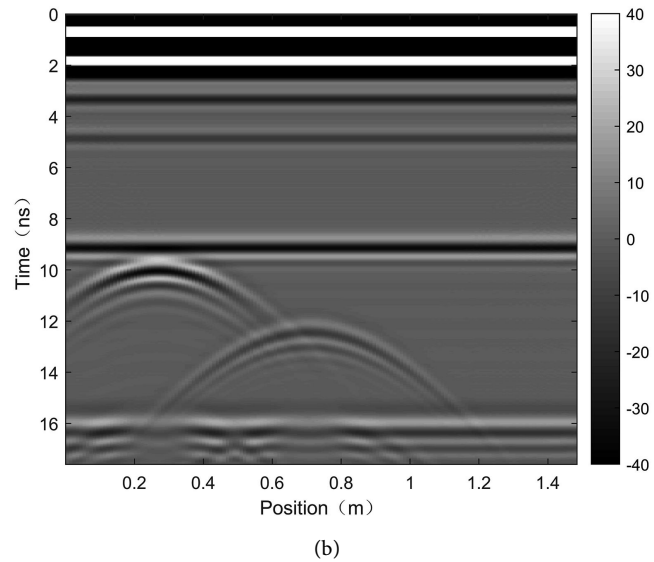


Figure 13. (a) Dielectric model of pavement with undercompacted base bottom; (b) Reflected wave of model 13a.

Case 6: The dielectric model of pavement with poor bonding between base and surface course is shown in **Figure 14(a)**. One distress was contained in the model with the dimension of 1 cm \times 15 cm, and the corresponding reflected wave image is shown in **Figure 14(b)**.

Case 7: The dielectric model of pavement with poor bonding between base and subbase is shown in **Figure 15(a)**. One distress existed with the dimension of 0.5 cm \times 15 cm, and the corresponding reflected image is shown in wave **Figure 15(b)**.

Case 8: The dielectric model of pavement with poor bonding between subbase and subgrade is shown in **Figure 16(a)**. One distress existed with the dimension of 0.25 cm \times 15 cm, and the corresponding reflected wave image is shown in **Figure 16(b)**.

As can be seen from Case 6 - Case 8, the set bonding conditions got weaker from the top to the bottom of pavement structures, while the defects still could generally be revealed through the simulation wave images.

Case 9: The dielectric model of pavement with a crack in surface course is shown in **Figure 17(a)**. One distress (*i.e.*, a vertical crack) existed with the dimension of 15 cm \times 1 cm. The corresponding reflected wave is shown in **Figure 17(b)**, and it indicates that the vertical crack could also be identified through the reflected wave image.

Overall, it can be concluded that the position of abnormal zones in each layer had no (or slight) effects on the detection feasibility. For a certain dimension, the reflected wave images varied when the distresses were in different positions in each layer. In contrast, the detection accuracy of 900 MHz was superior to that of 400 MHz. 900 MHz antenna could also be employed to identify smaller defects. The poor bonding and vertical cracks could also be detected through the reflected wave images, besides voids and under compacted zones.

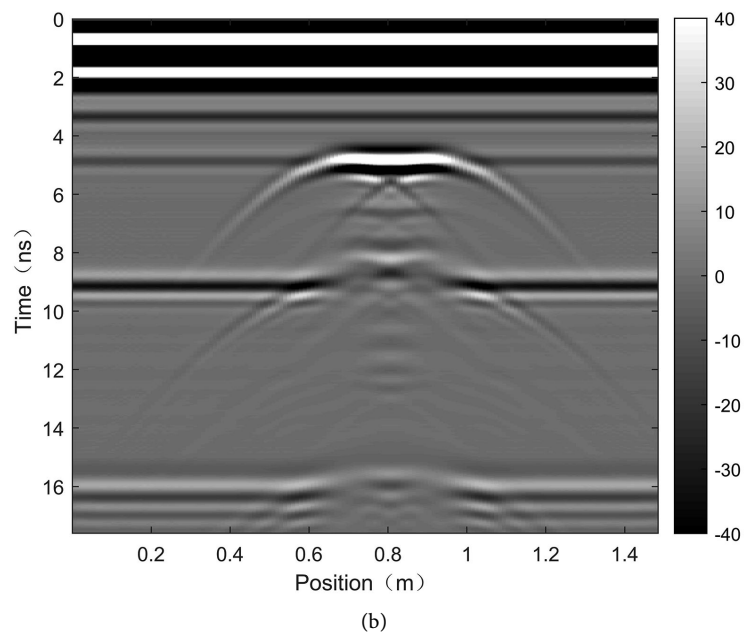
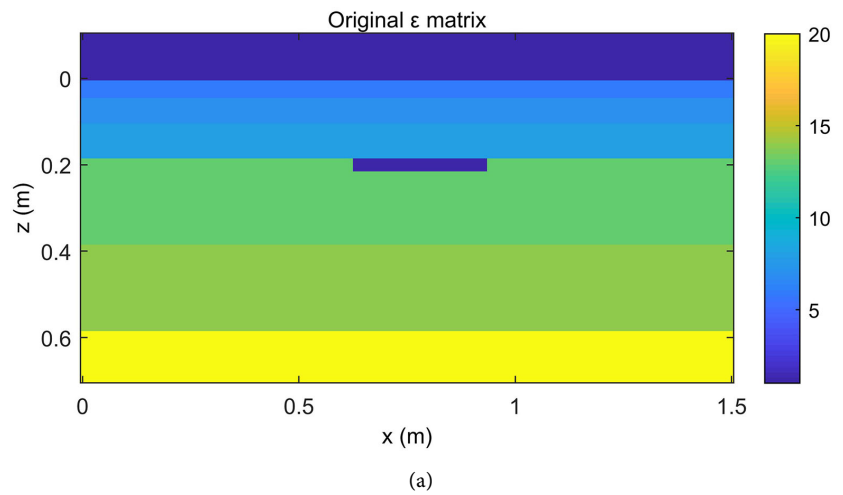
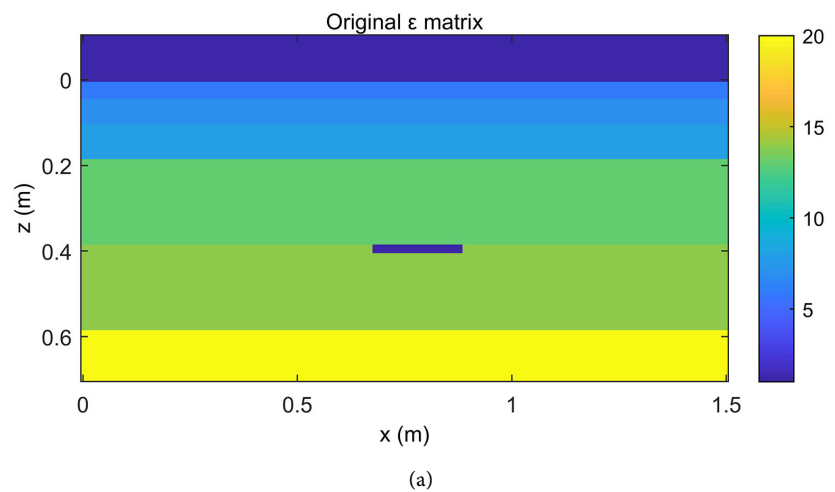


Figure 14. (a) Dielectric model of pavement with poor surface-base bonding; (b) Reflected wave of model 14a.



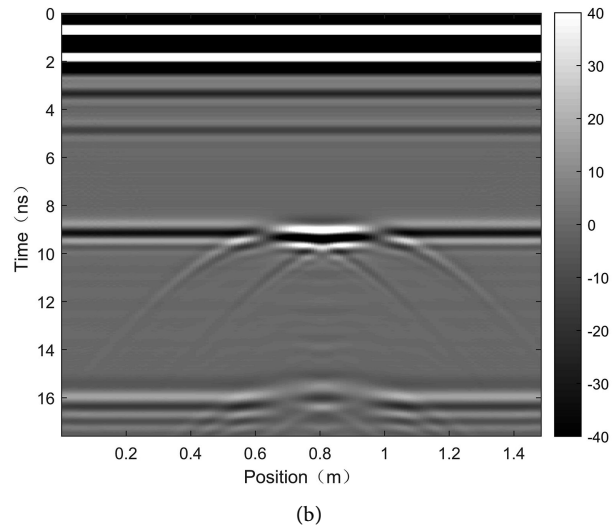


Figure 15. (a) Dielectric model of pavement with poor bonding between base and sub-base; (b) Reflected wave of model 15a.

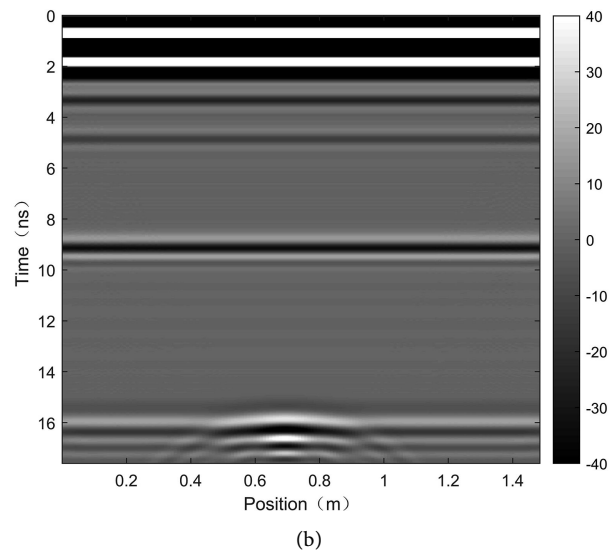
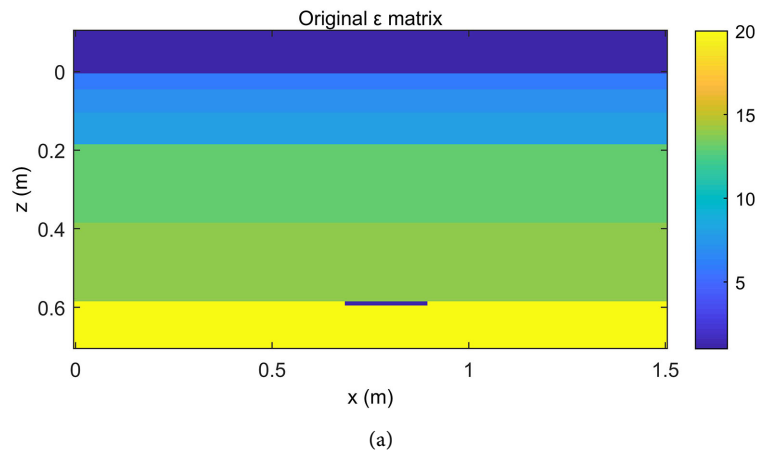


Figure 16. (a) Dielectric model of pavement with poor subbase-subgrade bonding; (b) Reflected wave of model 16a.

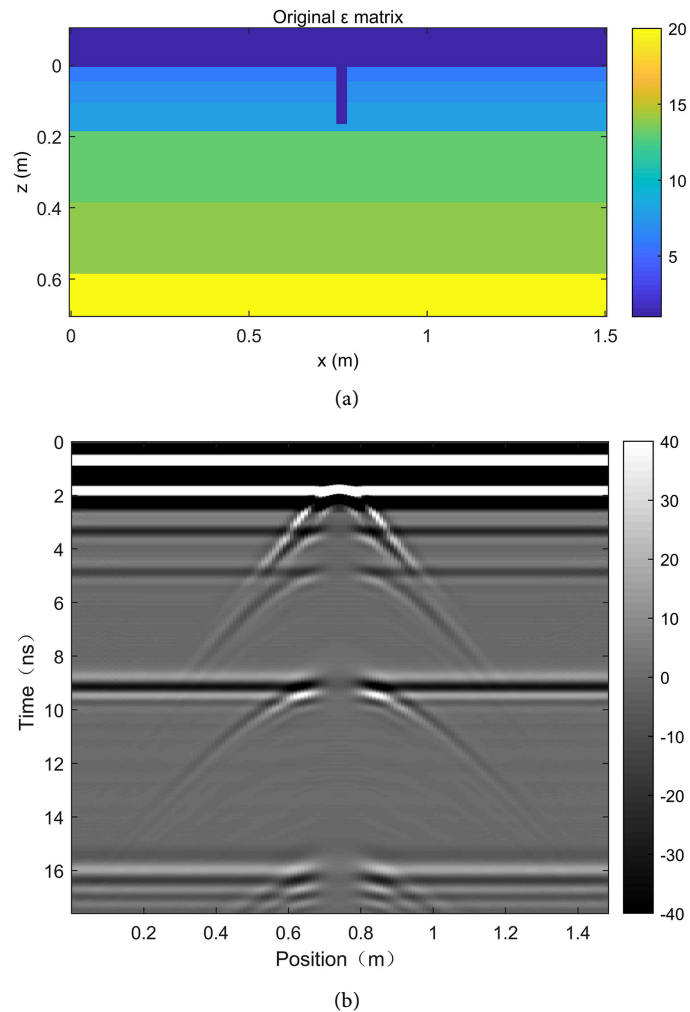


Figure 17. (a) Dielectric model of pavement with crack in surface course; (b) Reflected wave of model 17a.

3. Field Tests

An expressway extends from Airport to Heao in Shenzhen. When it is subjected to a period of traffic loads, some defects appear on the surface, e.g., settlement, rutting and cracks. The pavement performance will be impaired, endangering traffic safety. Thus, the surveying line is arranged in the left and right wheel path respectively at each lane, and the GPR method is used to detect internal defects in subgrade and other pavement structures.

GSSI Company's SIR-20 GPR was employed in the detection, and the 400 MHz ground-coupled antenna detection was conducted to obtain the related data about all the pavement structures up to the depth of 1.5 m. The sampling was continuous with a spacing of 2 cm, and positioning was achieved through odometer. The time window was set as 70 ns, and the gain was exponential. GPR images were collected along the direction of the lane. The polarisation direction of antenna was perpendicular to the direction of collecting images. Besides, the roadmap images were collected at a speed of 20 - 30 km/h.

The collected signals were gained and filtered, and background noise could be subtracted. Therefore, GPR data interpretation and visualization software for pavements was introduced to detect layer interfaces and abnormal zones, and transform the time scale of acquired GPR data into depth scale.

The normal output was a 2-D GPR image with horizontal and vertical axes representing distance and time respectively. The image contained all acquired traces plotted at the appropriate position. Through the comparison, test results got good agreement with core sampling results, and it was revealed that the test and detection method could be utilized to investigate pavement deep distresses.

The GPR image, pavement surface before coring and coring sample near K2876 + 082 (*i.e.*, test point) are shown in **Figure 18**. The pavement surface was in a relatively good condition except a small transverse crack. It can be seen from the GPR image that the surface course was nearly integrated from +076 to +090, while the bond between surface course and base was poor. Besides, moist and loose zones were also identified in the subgrade. At +078, a crack ran the length of the base. The coring samples from various layers (*i.e.*, the relatively integrated surface course, base with cracks, and loose zones between surface course and base) got good agreement with the acquired results from GPR images.

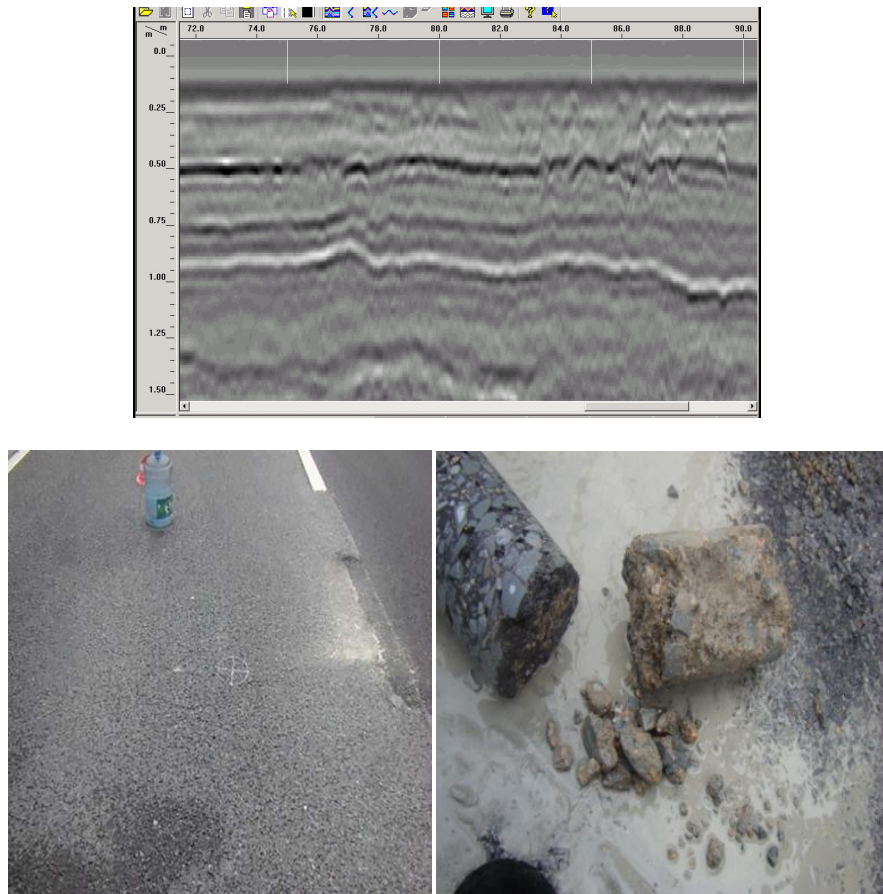


Figure 18. GPR image and coring sample at K2876 + 078 of upward carriageway.

Similarly, another test at K2878 + 010 was performed, as shown in **Figure 19**. The pavement surface course contained no distresses before coring, while, it can be seen from the GPR image that the surface course was partly integrated from +003 to +018. Besides, the bond between surface course and base was poor, and the loose zones were generated in the base and subbase. Particularly, both moist and loose zones existed in the subgrade. The coring samples from various layers (*i.e.*, the partly integrated surface course, the loose and poor bonding base) got good agreement with the acquired results from GPR images.

The SIR-20 type 900 MHz ground-coupled antenna GPR was employed in a testing pavement in Luohe, Henan province, and the investigation was conducted to obtain precise data about the whole pavement structures up to the depth of 1.0 m. The sampling was continuous with a spacing of 2 cm. The positioning was achieved through odometer. The time window was set as 50 ns. The field gain was adopted as exponential type. GPR images were collected along the driving direction of the roadway. The antenna polarisation direction was perpendicular to the collection direction of images. The pavement structure materials and composition are listed in **Table 2**.

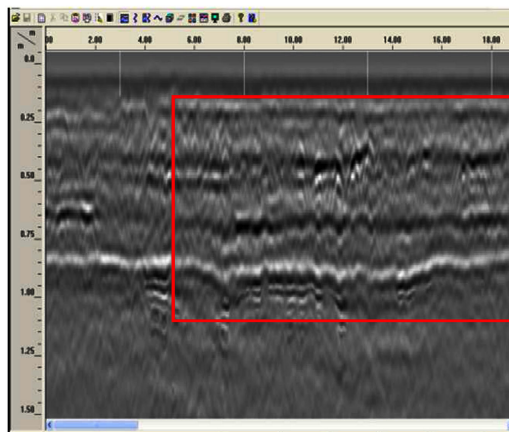




Figure 19. GPR image and coring sample at K2878 + 010 of downward carriageway.

Table 2. Pavement material and composition.

Layer	Table Column Head
1	3 cm fine-grained asphalt concrete (AC-13C)
2	5 cm medium-grained asphalt concrete (AC-20C)
3	0.5 cm slurry seal
4	17 cm lime stabilized soil gravel base
5	35 cm 12% lime stabilized soil subbase
6	semi-infinite subgrade

The surface course in the left side of left lane was severely damaged and fragmented, whose GPR images and coring samples are shown in **Figure 20**. It can be seen from the GPR image that the lime stabilized soil gravel base was loose and undercompacted, and some interlayers were also contained. The core sampling demonstrated that the thickness of surface course was insufficient, and some defects existed in the base. Although the surface course got destructed, the actual distress lay in the deep base.

The surface course in right side of right lane was slightly damaged, whose GPR images and coring samples are shown in **Figure 21**. It can be seen from **Figure 21** that the lime stabilized soil gravel base was nearly integrated, and some loose zones were created in lime stabilized soil subbase. The bond between surface course and base was poor, and the bond between base and subbase was also poor. The core sampling revealed that the thickness of surface course was insufficient, and the surface course and base was detached. Therefore, it can be seen from the GPR image that the induced distresses existed in deep base or subbase, besides the surface diseases.

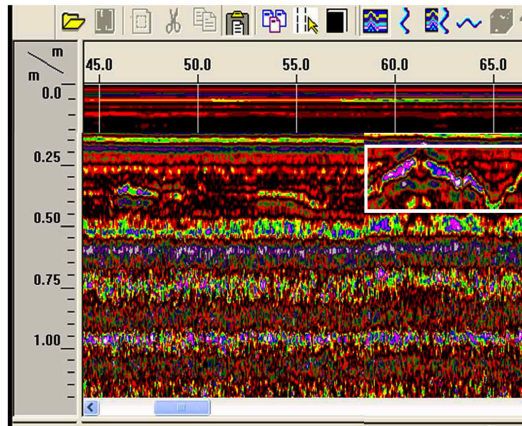


Figure 20. GPR image and coring sample at K1 + 062 in the left side of left lane.

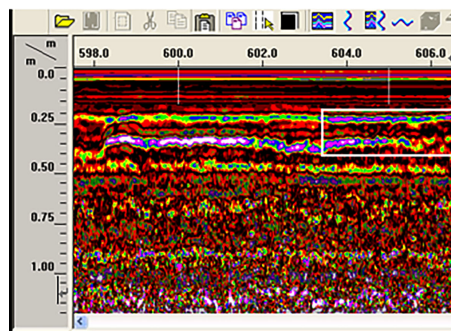


Figure 21. GPR image and coring sample at K0 + 602 in right side of right lane.

4. Case Study

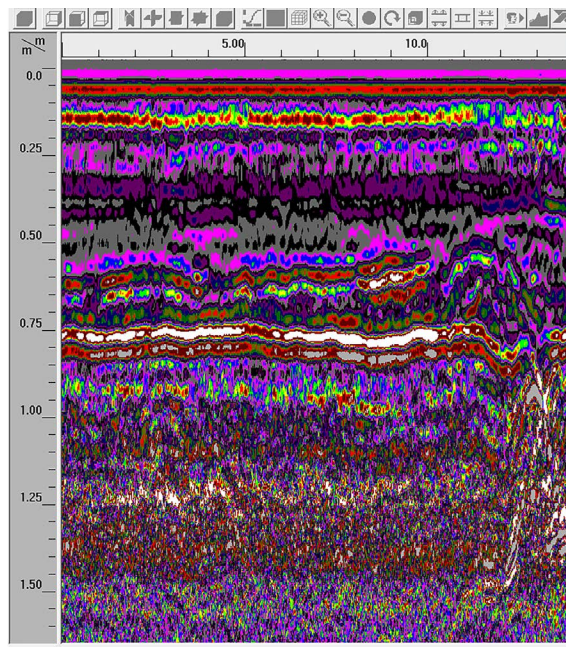
The GPR images at K2900 + 600 - K2900 + 615 of upward carriageway in Shenzhen Expressway from airport to Heao are presented in **Figure 22**. From K2900 + 603 to K2900 + 615 at the depth range of 0.18 - 0.22 m, 0.45 - 0.6 m and 0.60 - 0.85 m, the abnormal zones were illustrated in **Figure 22**. Furthermore, some defects were determined lying in the base and subbase, and photos of the corresponding layers with defects are shown in **Figure 23** and **Figure 24**.

Some defects (e.g., longitudinal cracks, transverse cracks, block, loose zones, and local infiltration) could be seen from **Figure 23**. The loose zones and local infiltration could be found in **Figure 24**. Therefore, the deep defects in base and subbase could be identified by GPR quite probably.

The GPR image at K2902 + 980 - K2903 + 000 of upward carriageway in Shenzhen expressway from airport to Heao is shown in **Figure 25**. From K2902 + 985 to K2902 + 999 at the depth range of 0.18 - 0.23 m, 0.4 - 0.6 m and 0.60 - 0.75 m. Some abnormal sections are presented in **Figure 25**. Some defects were determined lying in the base and subbase, and photos of the corresponding layers with defects are shown in **Figure 26** and **Figure 27**.

Some defects (e.g., longitudinal cracks, transverse cracks, block, loose zones, and local infiltration) could be seen from **Figure 26**. The loose zones and local infiltration could be found in **Figure 27**. Therefore, the deep defects in base and subbase could be identified by GPR quite probably.

Based on the simulation and field verification, the position, type and layer of the distress were determined for the Shenzhen Expressway from airport to Heao. A portion of test results are presented in **Table 3**. Thus, the corresponding treatment should be considered before maintenance according to various distresses.



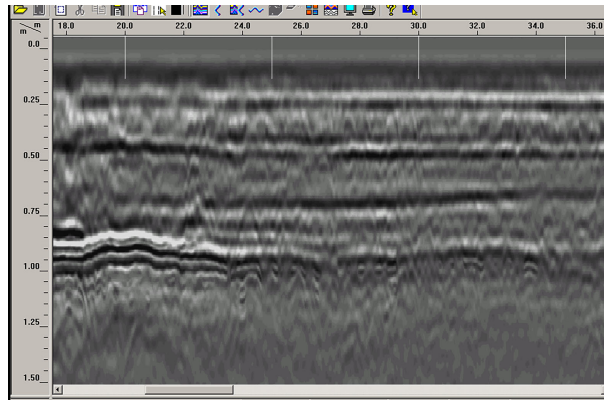


Figure 22. GPR image at K2900 + 600 - K2900 + 615 of upward carriageway.



Figure 23. Photo of top base at K2900 + 605 - K2900 + 610.





Figure 24. Photo of top subbase at K2900 + 605 - K2900 + 610.

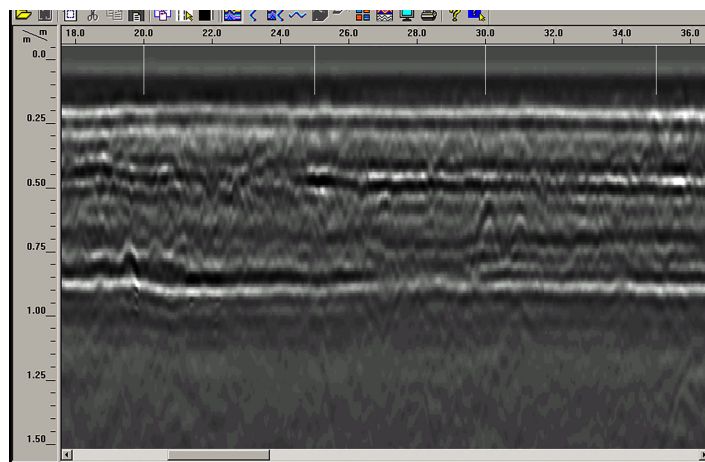
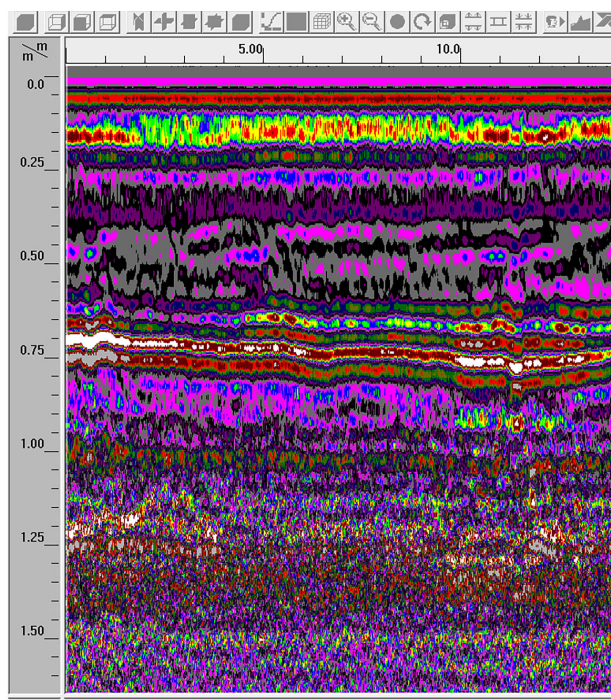


Figure 25. GPR image at K2902 + 980 - K2903 + 000 of upward carrieway.

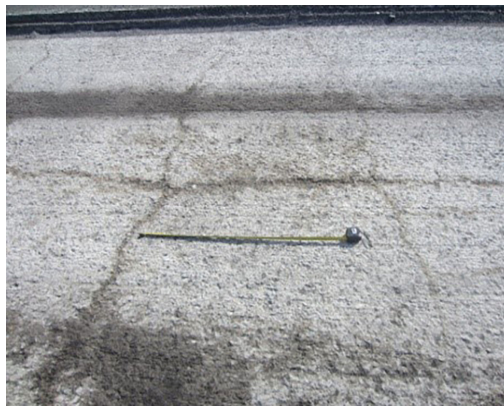


Figure 26. Photo of top base at K2900 + 605 - K2900 + 610.



Figure 27. Photo of top subbase at K2900 + 605 - K2900 + 610.

Table 3. GPR test results about Shenzhen Expressway.

Position	Starting position	Ending position	Distress	Comment
K2866 + 000 - K2866 + 100	82	102	Loose in bass	
K2866 + 100 - K2866 + 200	54	68	Uncompacted in base	
K2866 + 200 - K2866 + 300	84	112	Uncompacted in base	
K2866 + 300 - K2866 + 400	7	11	Loose in bass	
	22	29	Loose in subbase	
	36	48	Loose in bass	pipeline
	84	98	Loose in bass	
K2866 + 400 - K2866 + 500	0	16	Loose in subbase	
	22	34	Uncompacted in subbase	
	38	44	Loose in bass	
	56	64	Uncompacted in base	
K2866 + 500 - K2866 + 600	0	7	Loose in bass	
	20	26	Loose in bass	
	40	65	Uncompacted in subbase	
K2866 + 600 - K2866 + 700	21	30	Loose in bass	
	36	46	Loose in bass	
	74	86	Uncompacted in base	
	93	100	Loose in bass	
K2866 + 700 - K2866 + 800	20	42	Loose in bass	
	64	85	Uncompacted in base	pipeline
K2866 + 800 - K2866 + 900	52	76	Loose in bass	patch
K2866 + 900 - K2867 + 000	27	36	Loose in subbase	

5. Conclusions

Within various layers, one or several abnormal zones with different dimensions represented defects respectively. The defects induced different values of ε and σ in the corresponding pavement structures. Dielectric models of pavement structure layers were established.

The application of nondestructive GPR detection has become an integral part in the structural evaluation and rehabilitation process of pavements in recent years. As some deep distresses exist in pavement structures, GPR reflected waves varied at interfaces and the zones with defects.

In practice, GPR detection depth got smaller through the theoretical simulation, while pavement structures could be penetrated by 900 MHz or 400 MHz antenna. Thus, the deep distress could be identified from the reflected wave images quite probably.

Radar operating in 900 MHz and 400 MHz could be utilized to detect the deep

disease in pavement structures. Generally, 400 MHz antenna was mainly used to investigate the infrastructure, e.g., base and subgrade, while 900 MHz antenna was mainly employed to detect base and subbase.

Based on different situations, the appropriate antenna and time window were set to guarantee detection depth and accuracy. In pavement deep distress detection, the 400 and 900 MHz antennas were applicable, except focusing on different structural layers.

Conflicts of Interest

The authors declare no conflicts of interest regarding the publication of this paper.

References

- [1] Lahouar, S. and Al-Qadi, I.L. (2008) Automatic Detection of Multiple Pavement Layers from GPR Data. *NDT&E International*, **41**, 69-81.
<https://doi.org/10.1016/j.ndteint.2007.09.001>
- [2] Guo, C.-C. and Wang, F.-M. (2008) Study on Forward Modeling of GPR Electromagnetic Wave Propagation. *Journal of Highway and Transportation Research and Development*, **25**, 37-41. (In Chinese)
- [3] Parrilla, D.V. (2006) GPR for Road Monitoring and Damage Detection: The Layer-Stripping Algorithm. Master Thesis, Università degli studi Roma Tre, Roma.
- [4] Saarenketo, T. and Scullion, T. (2000) Road Evaluation with Ground Penetrating Radar. *Journal of Applied Geophysics*, **43**, 119-138.
[https://doi.org/10.1016/S0926-9851\(99\)00052-X](https://doi.org/10.1016/S0926-9851(99)00052-X)
- [5] Tosti, F. and Benedetto, A. (2012) Pavement Pumping Prediction Using Ground Penetrating Radar. *Procedia—Social and Behavioral Sciences*, **53**, 1045-1054.
<https://doi.org/10.1016/j.sbspro.2012.09.954>
- [6] Mardeni, R., Raja Abdullah, R.S.A. and Shafri, H.Z.M. (2010) Road Pavement Density Analysis Using a New Non-Destructive Ground Penetrating Radar System. *Progress in Electromagnetics Research B*, **21**, 399-417.
- [7] Diamanti, N. and Redman, D. (2012) Field Observations and Numerical Models of GPR Response from Vertical Pavement Cracks. *Journal of Applied Geophysics*, **81**, 106-116. <https://doi.org/10.1016/j.jappgeo.2011.09.006>
- [8] Krysiński, L. and Sudyka, J. (2013) GPR Abilities in Investigation of the Pavement Transversal Cracks. *Journal of Applied Geophysics*, **97**, 27-36.
<https://doi.org/10.1016/j.jappgeo.2013.03.010>
- [9] Evans, R. (2008) A Review of Pavement Assessment Using Ground Penetrating Radar (GPR). *12th International Conference on Ground Penetrating Radar*, Birmingham, 16-19 June 2008.
- [10] Irving, J. and Knight, R. (2006) Numerical Modeling of Ground-Penetrating Radar in 2-D Using MATLAB. *Computers & Geosciences*, **32**, 1247-1258.
<https://doi.org/10.1016/j.cageo.2005.11.006>